This article has been accepted for inclusion in a future issue of this journal. Content is final as presented, with the exception of pagination.

Investigation of the Internal Back Reflectance of Rear-Side Dielectric Stacks for c-Si Solar Cells

Kristopher O. Davis, *Member, IEEE*, Kaiyun Jiang, Carsten Demberger, Heiko Zunft, Helge Haverkamp, Dirk Habermann, and Winston V. Schoenfeld

***Abstract*—This paper addresses the calculation of internal back reflectance for various dielectrics that are used in rear-side passivated crystalline silicon solar cells. Optical modeling of various stack configurations is examined to explore the back-surface reflectance at the Si–dielectric interface for different film combinations and thicknesses as a function of wavelength and internal angle of incidence at the rear side. Specifically, configurations using aluminum oxide (AlO_x), silicon nitride (SiN_x), titanium dioxide (TiO_2), and silicon dioxide (SiO_2) were investigated with a focus on designing stack configurations that will also allow for high-quality passivation and are compatible with a high-volume manufacturing environment. In addition, samples were fabricated by plasma-enhanced and atmospheric pressure chemical vapor deposition of thin dielectric films onto polished and textured monocrystalline silicon wafers. Spectral reflectance curves of the samples are presented to supplement and validate the conclusions that are obtained from the optical modeling data.**

***Index Terms*—Characterization, dielectric films, metrology, optics, photovoltaic cells, silicon, Si photovoltaics (PV) modeling.**

I. Introduction

THE transition to thinner silicon wafers (e.g., < 150 μm) in crystalline silicon (c-Si) photovoltaics (PV) offers the potential for significant advantages in terms of both performance (e.g., higher open-circuit voltages due to reduced bulk recombination [1], [2]) and cost (e.g., improved silicon usage efficiency [3]–[5]). However, there are still many challenges that are associated with processing thin silicon wafers including wafer handling [6], wafer bowing when using a full Al back contact [7], surface recombination at the backside of the cell [8], and reduced absorption of near-bandgap photons [9].

In-line deposition of rear-side dielectric passivation layers has emerged as a strong candidate to realize passivated emitter and rear cell (PERC) solar cells, which address the issues of wafer bowing and rear-side surface recombination, while also offering light trapping advantages for weakly absorbing wavelengths due to increased internal back reflectance (IBR) when compared with standard aluminum back surface field (Al-BSF) cells [10], [11]. This paper focuses on modeling IBR at the Si-dielectric interface for various dielectric stack configurations. Higher reflectance effectively increases the optical path length of the cell, which can lead to increased absorption, particularly at longer wavelengths (900–1120 nm), which are poorly absorbed in c-Si due to the indirect bandgap. This is highlighted in Fig. 1, where the fraction of light absorbed in c-Si as a function of wavelength is given for four different optical path lengths (1 mm, 200 μm, 50 μm, and 10 μm) using published absorption coefficient data [12]. The effective optical path length of a solar cell is dependent on the wafer thickness and overall light trapping ability of the cell.

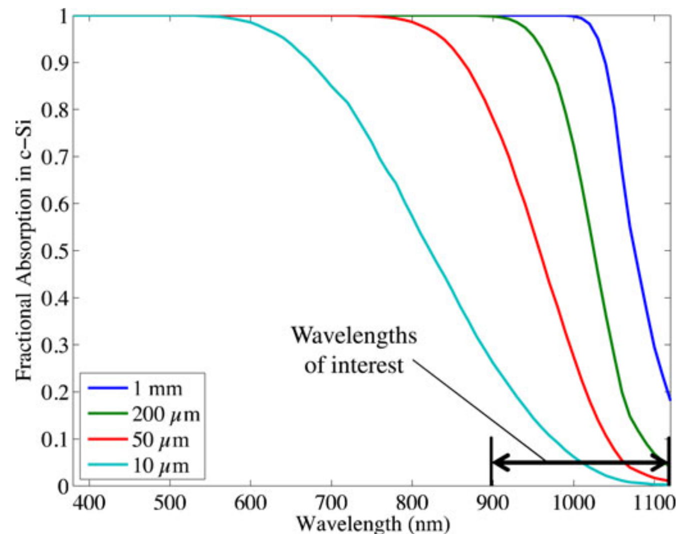

Fig. 1. Fractional absorption in c-Si for four different optical path lengths: 1 mm, 200 μm, 50 μm, and 10 μm.

AlO_x has gained significant attention as a rear-side passivation material for p-type c-Si solar cells. Surface recombination velocities below 5 cm/s have been achieved with this material [13]–[15], resulting in significant interest from the PV community of late. In an industrial PERC-type cell design, the thin AlO_x film will likely require a capping layer to prevent the screen-printed Al paste from penetrating through AlO_x [16]. Therefore, dielectric stack configurations using AlO_x have recently been explored experimentally, including AlO_x–SiO_2 and AlO_x–SiN_x [16]–[21]. The double-layer dielectric coating (DLDC) configurations that are considered in this simulation study all consist of an AlO_x passivation layer of at least 10 nm thick to ensure compatibility with well designed p-type PERC cells,

Manuscript received September 7, 2012; revised November 20, 2012; accepted December 5, 2012.

K. O. Davis and W. V. Schoenfeld are with the Florida Solar Energy Center and the College of Optics and Photonics, University of Central Florida, Orlando, FL 32826 USA (e-mail: kdavis@ fsec.ucf.edu; winston@fsec.ucf.edu).

K. Jiang, C. Demberger, H. Zunft, H. Haverkamp, and D. Habermann are with the Gebr. Schmid GmbH & Company, Freudenstadt 72250, Germany (e-mail: Jiang.Ka@schmid-group.com; Demberger.Ca@schmid-group.com; Zunft.He@schmid-group.com; Haverkamp.He@schmid-group.com; Habermann.Di@schmid-group.com).

Color versions of one or more of the figures in this paper are available online at http://ieeexplore.ieee.org.

Digital Object Identifier 10.1109/JPHOTOV.2012.2233861

2156-3381/$31.00 © 2012 IEEE

This article has been accepted for inclusion in a future issue of this journal. Content is final as presented, with the exception of pagination.

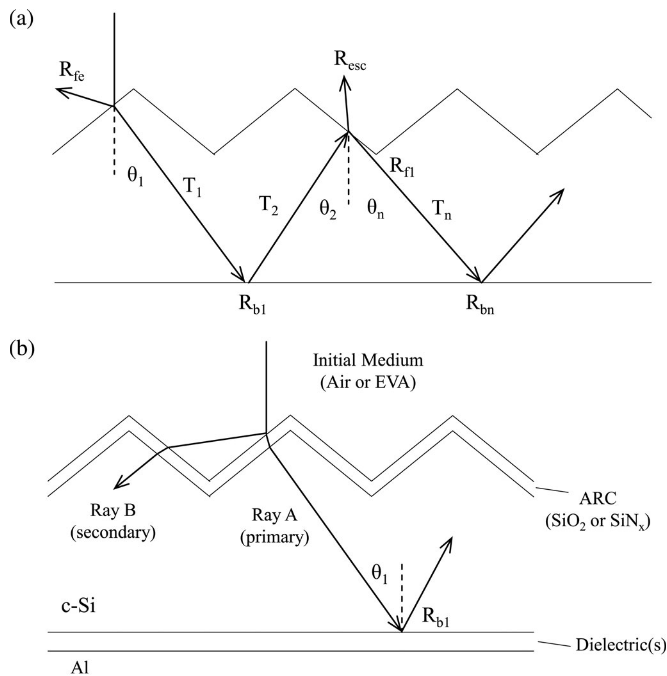

Fig. 2. Schematics illustrating the key optical parameters of interest. (a) Basore optical model, from [23]; (b) two primary transmitted rays in a textured monocrystalline solar cell, from [24]. Note: θ_1 of the primary ray for an encapsulated cell is smaller (35°) than that of an unencapsulated cell (41.4°).

in terms of effective chemical and field-effect passivation (see Fig. 2). DLDCs featuring SiN_x, TiO_2, and SiO_2 capping layers are all investigated. This study expands on recently presented results [22] by providing more simulation data and analysis as well as includes experimental data to supplement and validate the conclusions that are obtained from the modeling. As with the previous study, a planar backside is assumed.

II. Optical Modeling Methodology

A popular model to characterize the IBR of c-Si solar cells was introduced by Basore, see Fig. 2(a), and relies on the utilization of experimentally measured internal quantum efficiency (IQE) data of c-Si cells and calculates the aggregate IBR over all relevant wavelengths [23]. Later, more detailed investigation of IBR by Kray *et al.* used raytracing software and IQE data to empirically determine IBR (again to be an aggregate value with respect to λ and for radiation incident normal to the surface) [24].

This study has been carried out by first directly calculating IBR irrespective of the cell electronic properties, similar to the treatment by Green [25], but expanded to include multiple materials, stack configurations, and different frontside optics (e.g., with and without encapsulation). The IBR of these configurations is calculated for different angles of incidence between the silicon and initial dielectric layer (θ_1) and averaged over four near-infrared (NIR) wavelengths (λ = 900, 950, 1000, 1050 nm). The goal is to provide new insight and a starting point for comparing the various dielectric configurations in terms of IBR enhancement. A MATLAB program was created to implement the transfer matrix method (TMM) of calculating multilayer transmission and reflectance [26]. Randomly polarized light incident on random, 3-D upright pyramids is assumed in the TMM calculations. The pyramid features are assumed to be much larger than the wavelengths of interest here; therefore, diffractive effects are ignored. TE and TM components were calculated separately, and equal components of each were used to determine reflectance at the Si-dielectric interface.

TABLE I
NIR Refractive Index Values Used for TMM Calculations

Dielectric Layer	*Refractive Index*
AlO_x	1.63 [28]
Thermal SiO_2	1.45 [27]*
TiO_2 (low temp. anneal)	2.05 [29]**
TiO_2 (high temp. anneal)	2.42 [29]**
SiN_x	2.06**

*Measurements of *n* and *k* performed on the APCVD SiO_2 films used in the experimental part of this study showed excellent agreement with published data for thermal SiO_2.
**It should be noted that the refractive index of TiO_2 and SiN_x changes significantly depending on process conditions.

In this treatment, the dielectric layers are assumed to be lossless ($k = 0$) with a constant refractive index at the wavelengths of interest in this study (i.e., NIR). The assumed values are given in Table I and have been taken from both the literature [27]–[29] and ellipsometry measurements that are carried out on films deposited by atmospheric pressure chemical vapor deposition (APCVD) and plasma-enhanced CVD (PECVD). The complex refractive index parameters for the c-Si [12] and Al [30] layers were used throughout the calculations to account for losses due to the evanescent wave occurring for angles beyond the critical angle (θ_c). This last point is crucial, since the critical angle between Si and AlO_x is ≈26.5° ($n_{AlOx} = 1.63$, λ = 1000 nm) and θ_1 for most of the radiation on the backside is larger than this. This means that the surface wave and evanescent losses are the dominant loss mechanisms for IBR with these types of cell configurations. It should also be noted that for industrial c-Si solar cells using a screen-printed Al paste, the actual n and k values likely deviate from that of pure Al, even though those are the values that are commonly used. The authors are currently investigating this issue and plan to present the results in a future publication.

For textured monocrystalline wafers, the characteristic base angle (α) of the well-known pyramid structures is commonly taken to be 54.74°, although recent work has shown that in industrial cells this is actually around 50–52° depending on the etchant used [31]. Assuming $\alpha = 54.74°$ and a SiO_2 frontside coating, Kray *et al.* show that at normal incidence, the two primary rays that are transmitted through the cell have θ_1 of 41.4° and 59.1°, the former (Ray A) being the primary ray, which carries 76.4% of the total incident flux, and the latter (Ray B) carrying 19.4% [24]. This is illustrated in Fig. 2(b). It should be noted that the frontside texture does affect θ_1, both in terms of the types of pyramids and α. Ray tracing data for regular upright, inverted, and random upright pyramids can be found in [32]. Using simple geometrical optics equations, one can show that the primary ray for a similar cell with a SiN_x antireflection coating (ARC) has an equivalent θ_1. However,

This article has been accepted for inclusion in a future issue of this journal. Content is final as presented, with the exception of pagination.

θ_1 of the primary ray for an encapsulated cell is significantly lower at ≈35° ($n_{\mathrm{EVA}} = 1.5$, $n_{\mathrm{SiNx}} = 2.2$). Since the reflectance contour plots given in Section IV are given as a function of both dielectric thickness and θ_1 (from 0° to 60°), they can be used to determine IBR for different transmitted ray angles.

In addition to the TMM reflectance calculations that are executed in MATLAB, the freeware optical calculator named OPAL 2 and its built-in complex refractive index library were also used to investigate the wavelength dependent IBR for different dielectric stack configurations [33].

III. Experimental Details

Test samples have been fabricated to supplement and validate the results and conclusions that are obtained from the optical modeling. For these experiments, two different wafer types have been used: 250-μm-thick, 6-in round FZ p-type wafers with 2 Ω·cm resistivity and both sides polished and optically smooth; and 180-μm-thick, 156-mm square-mono-CZ p-type wafers with 1–3 Ω·cm resistivity, a frontside textured via an alkaline-based solution (i.e., anisotropically etched) and the backside chemically polished via a HF/HNO_3 solution. The round, polished FZ wafers and a portion of the textured CZ wafers were cut into smaller pieces using a laser treatment system. AlO_x, SiO_2, and TiO_2 films of varying thickness were deposited on the backside of substrates using an industrial, inline APCVD system (Schmid Thermal Systems, formerly Sierratherm), while the SiN_x films were deposited on the front and back of the substrates that use a standard PECVD batch process. SiN_x antireflection coatings (ARC) were also deposited onto the frontside that uses PECVD; however, thicker ARCs (180–200 nm) were used to reduce the front surface reflection at the NIR wavelengths of interest in this study (as opposed to the conventional approach of broadband reflection suppression for solar cells). For the smaller pieces cut using the laser system, 200-nm Al films were deposited via thermal evaporation on the backside of the samples. For the full 156-mm wafers, a standard screen-printed Al paste was printed onto the backside and subsequently fired using an industrial belt firing furnace.

Ellipsometry measurements were also carried out to characterize the deposited dielectric films on the polished substrates using a SENTECH SE800 PV spectroscopic ellipsometer and a SENTECH SE400 laser ellipsometer (λ = 632.8 nm). The SiN_x films that are deposited on the textured substrates were characterized using a J. A. Woollam M-2000XI T-SOLAR system. The measured refractive index data were found to be in excellent agreement with the values that are used in these simulations and those found in the literature (<3% relative difference for the wavelengths of interest). Reflectance measurements were carried out using an Ocean Optics HR2000+ high-resolution spectrometer, Mikropack DH-2000-BAL light source, Mikropack integrating sphere, and Labsphere reflectance standards. Reflectance was measured for wavelengths between 250 and 1105 nm at ≈0.5 nm increments.

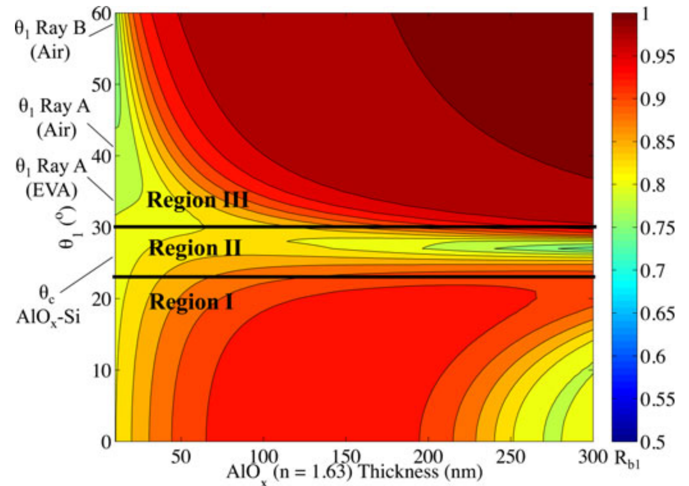

Fig. 3. IBR contour map for backside SLDC with AlO_x, highlighting the three regions of interest and the primary ray angles transmitted through the front surface of textured monocrystalline cells with and without encapsulation (noted as "EVA" and "Air," respectively).

IV. Results and Discussion

A. Transfer Matrix Method Contour Plots

By plotting contour maps of the IBR versus dielectric layer thickness and θ_1, some interesting trends can be seen. For example, there are three critical regions with respect to θ_1, as shown in Fig. 3.

1) *Region I* ($\theta_1 < \theta_c$): In this region, the electromagnetic wave propagates through the dielectric film(s) and interference effects play a key role in the resulting reflectance, hence the periodic dependence on layer thickness (constructive versus destructive interference). These smaller angles of incidence are less interesting for anisotropically etched monocrystalline cells, due to refraction of primary beams, but could be of interest in cells with different texturing and ARC configurations (e.g., black silicon).
2) *Region II* (θ_1 near θ_c): At the critical angle, total internal reflection occurs and rather than propagating into the film, the wave propagates parallel to the Si–AlO_x interface (i.e., surface wave) [34]. This surface wave that propagates parallel to the interface allows for rather efficient energy transfer to the lossy Al layer.
3) *Region III* ($\theta_1 > \theta_c$): As the angle of incidence increases above the critical angle, less energy is transferred to the Al layer. The energy carried by the evanescent wave propagating parallel to the Si–AlO_x interface is attenuated as the distance from the higher index media (i.e., Si) is increased. This attenuation is increased as θ_1 increases, and this is why the larger angles of incidence and thicker dielectric layers result in higher IBR.

In this case of a single-layer dielectric coating (SLDC) with AlO_x, the primary ray angles for cells with and without encapsulation fall within Region III. Therefore, layer thickness is not very critical, as long as it is beyond a certain thickness. Based on cost considerations, the fact that the passivation quality saturates after approximately 15 nm [35], and the fact that a capping layer

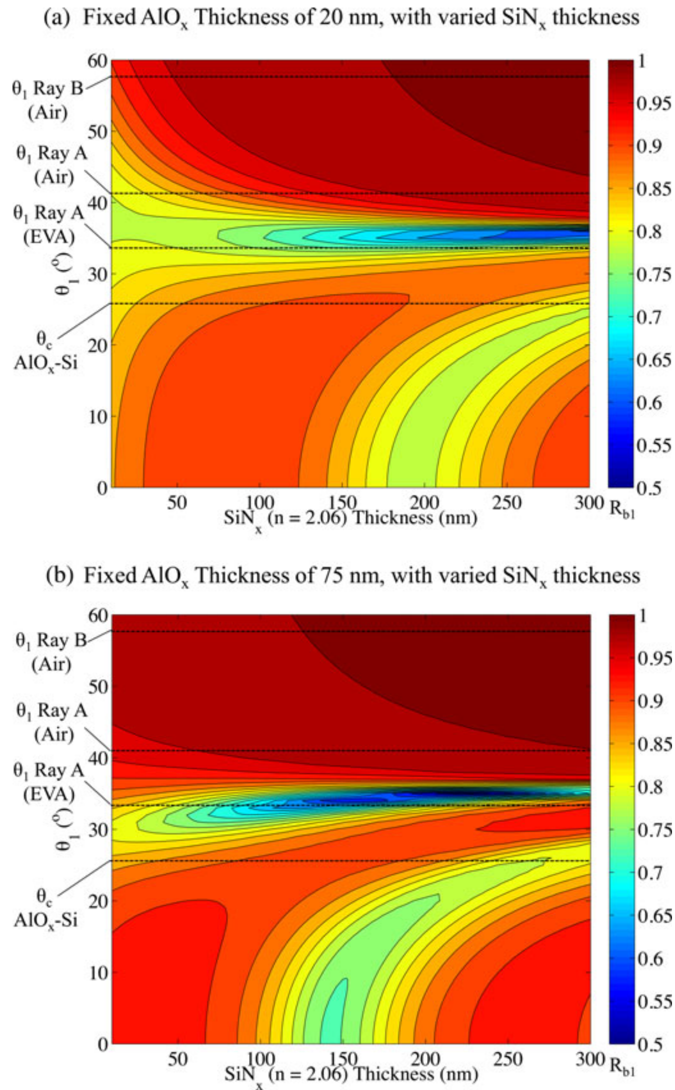

Fig. 4. IBR contour maps for backside DLDC with AlO_x–SiN_x as a function of SiN_x thickness and θ_1 for two fixed AlO_x thicknesses: (a) 20 nm and (b) 75 nm.

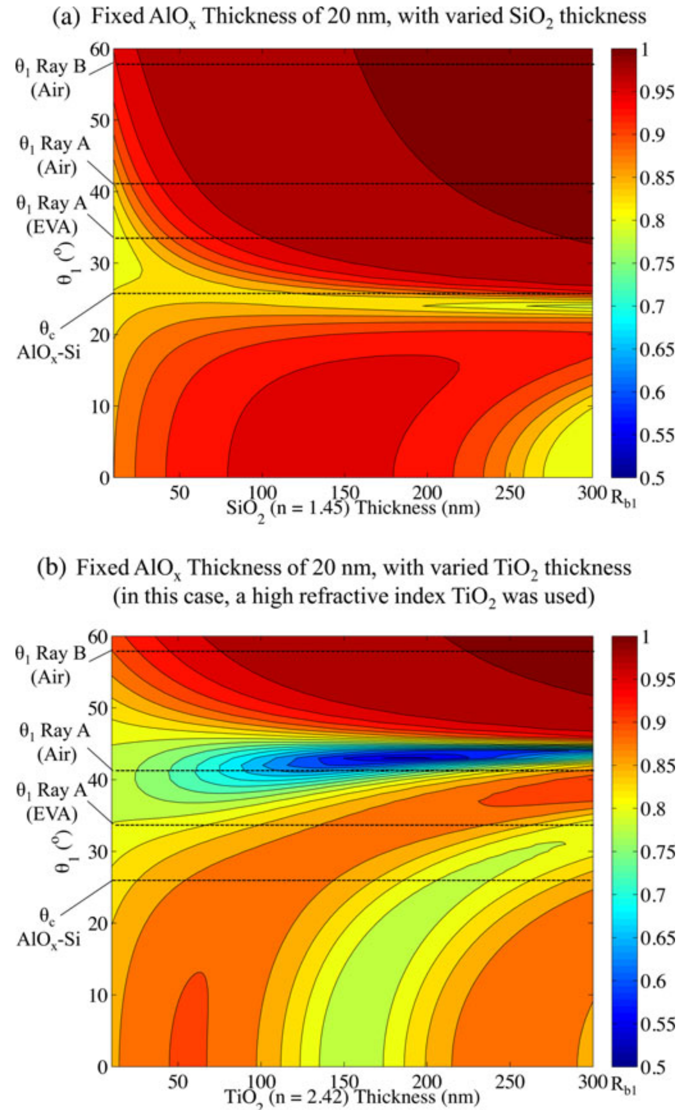

Fig. 5. IBR contour maps for backside DLDC with (a) AlO_x–SiO_2 and (b) AlO_x–TiO_2, with n taken from high temperature anneal TiO_2. Both configurations feature a fixed AlO_x thickness of 20 nm.

is required to protect the AlO_x from a screen-printed paste, the AlO_x film thickness should be limited.

As mentioned before regarding industrial PERC cell designs, a lower cost capping layer should be used to prevent the screen-printed Al paste from penetrating through AlO_x. It is known that the added thickness of this capping layer can also promote higher IBR, which has been shown experimentally on *unencapsulated* cells [24].

Fig. 4 shows IBR versus SiN_x capping layer thickness for two different fixed AlO_x thicknesses (20 nm, 75 nm). In this case, due to the higher index of refraction of SiN_x compared with AlO_x, the poorly reflecting Region II is effectively shifted to higher values of θ_1. While this does not significantly affect the unencapsulated cell case, it appears to reduce the IBR for encapsulated cells, which have a smaller θ_1. This suggests that an encapsulated PERC cell with a thick, higher index capping layer might not realize the same IBR enhancement (and therefore NIR IQE performance) as expected in the unencapsulated case.

Results for DLDC configurations with TiO_2 and SiO_2 capping layers have also been studied, both with a fixed AlO_x thickness of 20 nm (see Fig. 5). The lower refractive index of SiO_2 ensures that Region II is suppressed to values that are below that of the primary ray angles. It is known that the refractive index of TiO_2 can be varied widely depending on deposition temperature and postdeposition thermal treatments [29]. In this case, a high refractive index TiO_2 has been simulated, to illustrate the effect of a high-index capping layer on IBR. As expected, the lossy region in this case is pushed to higher values for θ_1.

The ray angle for additional passes through a cell (e.g., $\theta_2, \ldots, \theta_n$ in Fig. 2) is commonly assumed to be 60° to approximate the randomization of light rays through subsequent reflections at the front and rear sides of the cell [23]. In Fig. 3–5, it can be seen that IBR changes very little even for very large changes in

This article has been accepted for inclusion in a future issue of this journal. Content is final as presented, with the exception of pagination.

the dielectric layer thickness at this large angle. In Fig. 4(a) for example, changing the SiN_x capping-layer thickness from 50 to 175 nm, there is virtually no change in IBR at 60°. However, at 41.4° a $>10\%_{\mathrm{abs}}$ change in IBR is expected. This suggests that while subsequent reflections at the rear side of the cell (e.g., R_{bn} in Fig. 2) are quite important for the overall light trapping of a cell, ultimately the first reflection (R_{b1}) is much more dependent on the dielectric layer thickness and can, therefore, be controlled and optimized more readily.

B. OPAL 2 Calculations

Wavelength-dependent calculations of IBR have also been calculated, both for unencapsulated and encapsulated cells with six different configurations.

1) No dielectric.
2) SLDC with 30 nm-AlO_x.
3) SLDC with 50-nm-AlO_x.
4) DLDC with 20-nm AlO_x and 75-nm SiN_x.
5) DLDC with 20-nm AlO_x and 175-nm SiN_x.
6) DLDC with 20-nm AlO_x and 175-nm SiO_2.

As seen in Fig. 6(a), the results of the unencapsulated case are rather intuitive. Since the transmitted ray angle in this case is greater than the critical angle for any of the dielectrics used, the thicker stacks clearly perform better, due to more separation between the surface wave and the lossy Al layer. The results for the encapsulated case, shown in Fig. 6(b), are quite different though, matching the conclusions that are obtained by the TMM contour plots of IBR. In this case, the SiN_x-capped configurations have a lower IBR than even the no dielectric case. It should be noted again that the optical properties of pure Al, used here, vary from that of screen-printed Al. Additionally, screen-printed Al pastes result in rough interfaces and an intermediate Al–Si alloy layer [36], as opposed to the more planar interface of an evaporated Al film. As a reference, reported values for IBR have been included in both Fig. 6(a) –and (b), which are normally reported as wavelength-independent parameters [10], [21], [23], [24].

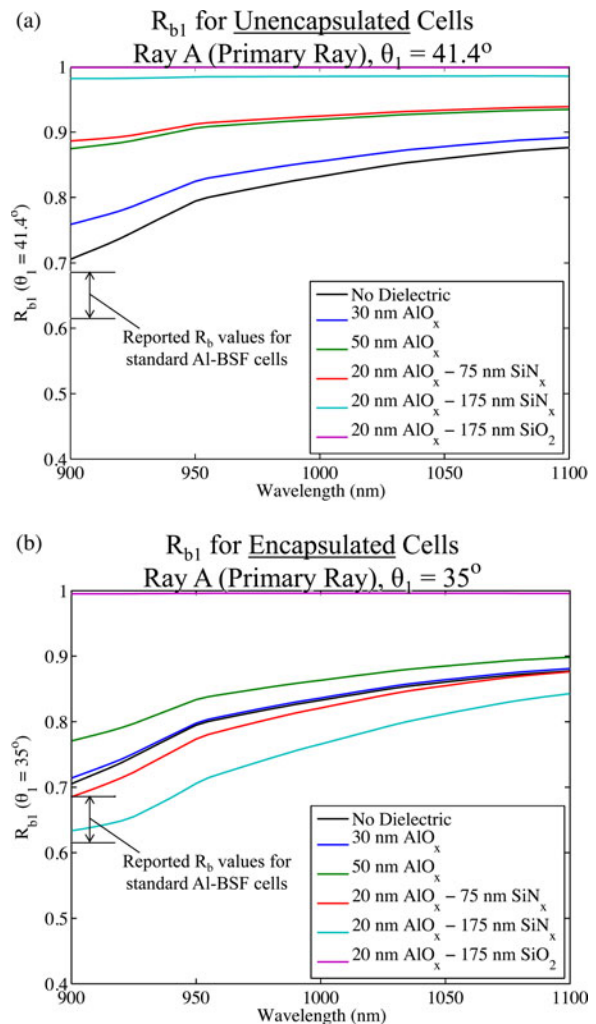

Fig. 6. Wavelength-dependent IBR, calculated using OPAL 2 for six different configurations for both (a) unencapsulated cells and (b) encapsulated cells.

C. Reflectance Measurements on Unencapsulated Cells

Referring to Basore's optical model that is shown in Fig. 2(a), the spectral reflectance measurements represent the sum of the front surface reflectance R_{fe} and the escape reflectance R_{esc}. R_{esc} is of interest in this study, since it is dependent on IBR. R_{fe} has been calculated as a function of wavelength using OPAL 2 and is included in the spectral reflectance curves that are presented in this study. This allows for a more straightforward comparison of R_{esc} and, therefore, the IBR. As expected, R_{fe} dominates the reflectance spectrum up to ≈1000 nm, since wavelengths that are lower than this are efficiently absorbed by the c-Si wafer for the wafer thicknesses used in these experiments (see Fig. 1).

The reflectance data for the polished, FZ wafers are shown in Fig. 7. Here, the results of four SLDC configurations are shown, three with AlO_x of increasing thickness and one with SiO_2. The SiO_2 SLDC shows the highest escape reflectance, and

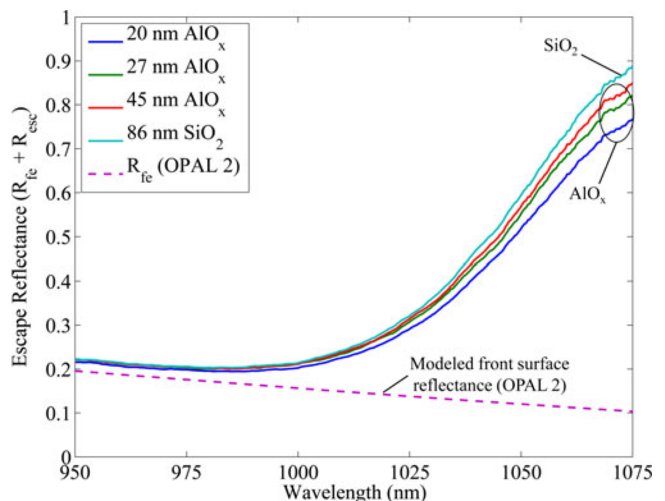

Fig. 7. Escape reflectance measurements shown for 950–1075 nm for four different unencapsulated SLDCs, one with SiO_2 and three with AlO_x of varying thickness, all with a planar front and rear side.

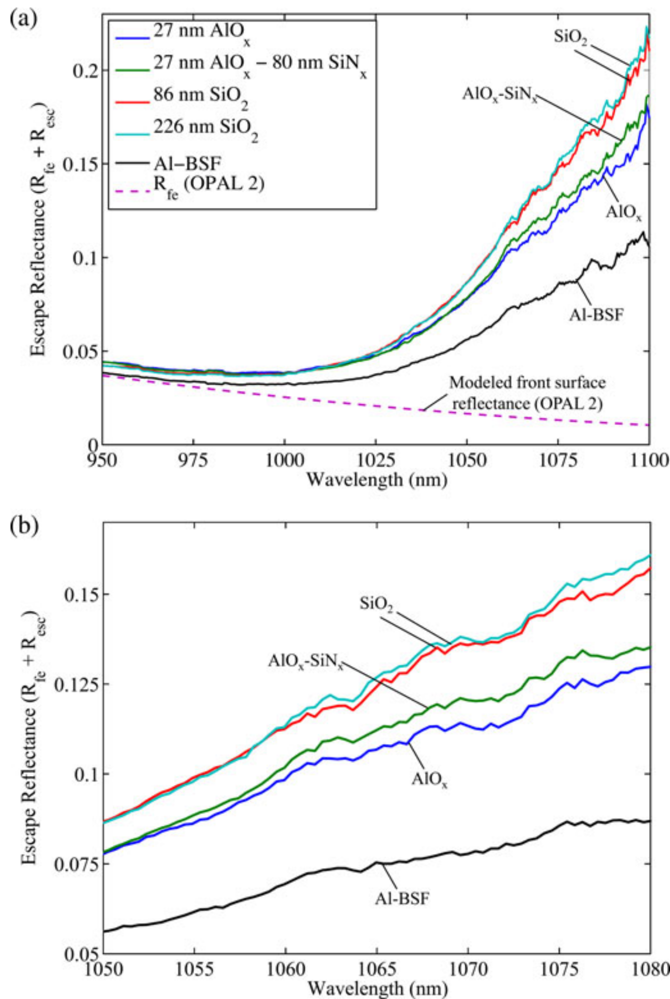

Fig. 8. Escape reflectance measurements performed on five different dielectric coating configurations with unencapsulated substrates with a textured front side and a planar rear side at (a) 950–1100 nm and (b) a zoomed-in view at 1050–1080 nm.

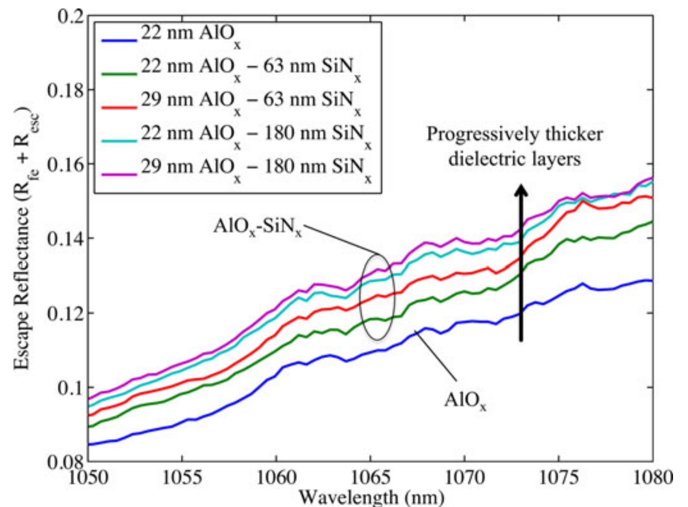

Fig. 9. Zoomed-in view (1050–1080 nm) of the measured escape reflectance of AlO_x–SiN_x coatings with different thicknesses, all performed on unencapsulated substrates with a textured front side and planar rear side.

for the AlO_x layers, the thicker films results in higher escape reflectance.

The experimental reflectance data for the textured samples showed good agreement with the conclusions that are made from the TMM contour plots and OPAL 2 calculations. Fig. 8 shows the measured escape reflectance for following unencapsulated test samples: standard Al-BSF; AlO_x; two SiO_2 samples; and an AlO_x–SiN_x DLDC sample. As expected, these substrates featured a much lower total reflection than the polished substrates due to the texturing of the frontside. The difference in the measured reflection data compared with IQE measurements of PERC cells can be explained by the thicker ARCs that are used in these experiments, which were used to suppress $R_{\rm fe}$ in the NIR region without concern for lower wavelength regions that are not of interest here (<900 nm). As expected, the SiO_2 coated samples have the highest escape reflectance, followed by the AlO_x–SiN_x sample, then the AlO_x coated sample, and the Al-BSF showing the lowest IBR. Fig. 9 shows a zoomed-in look at the IBR of various AlO_x–SiN_x samples, with a 22-nm AlO_x coated sample shown as a reference. Again, the trend of thicker coatings translates to higher escape reflectance for these unencapsulated test samples.

D. Modeled Impact on Maximum Achievable $J_{\rm SC}$

To calculate the impact of R_{b1} on the maximum achievable $J_{\rm SC}$, OPAL 2 has again been used. Both a specularly reflecting rear side and the Lambertian reflector on the rear side have been assumed. A specularly reflecting surface would be expected with a planar backside with pure Al (e.g., thermally evaporated), while more of a Lambertian reflection would be expected with rough rear surface and/or screen-printed Al paste. Two different wafer thicknesses have been investigated (30 μm, 180 μm). In all calculations, an unencapsulated, randomly textured front side ($\alpha = 54.74^\circ$) is assumed, with a 75-nm SiN_x ARC. Free carrier absorption in each case has been calculated assuming a ≈ 60 Ω/sq. emitter [37].

The maximum achievable $J_{\rm SC}$ has been determined by calculating the optical path length enhancement (Z) [38], [39] for varying values of R_{b1}, and is given in Fig. 10. Referencing Fig. 2, θ_1 is assumed to be 41.4° in both the specular and Lambertian cases. However, θ_2 is assumed to be 41.4° again for the specularly reflecting rear side, but 60° for the Lambertian reflector, a commonly used value to approximate a randomized distribution of rays [23]. Ray angles for all subsequent reflections, both at the front and rear sides, are assumed to be 60°, again using the randomization approximation.

The critical difference in modeling Z for the specular case versus the Lambertian case is that $R_{\rm f1}$ is much lower for the specularly reflecting rear side. This is due to the difference in θ_2. A large fraction of rays (more than half) are coupled out of the front side of the cell when the reflected ray angles are tightly distributed around 41.4°, as with the specular reflection. This leads to a lower Z parameter for the specularly reflecting rear side, and therefore a lower maximum $J_{\rm SC}$, when compared with the Lambertian case.

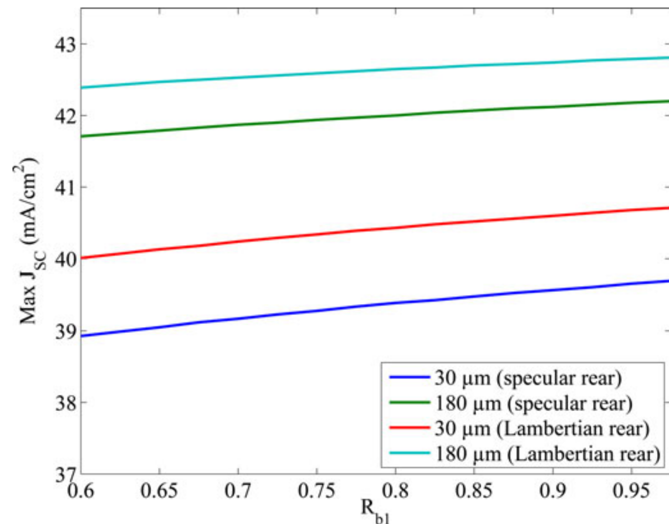

Fig. 10. Modeling results for maximum achievable J_{SC} as a function of R_{b1}.

For the 30-μm wafer, the maximum achievable J_{SC} is increased by 0.77 mA/cm^2 when going from R_{b1} of 60$\%_{\mathrm{abs}}$ to 97.5$\%_{\mathrm{abs}}$ for the specularly reflecting rear side and 0.70 mA/cm^2 for the Lambertian case. The impact of R_{b1} on J_{SC} is lower for the thicker 180-μm wafer. When going from R_{b1} of 60$\%_{\mathrm{abs}}$ to 97.5$\%_{\mathrm{abs}}$ for the 180-μm wafer, J_{SC} is increased by 0.49 and 0.42 mA/cm^2, for the specular and Lambertian cases, respectively. The following relationships give $\frac{\partial J_{\mathrm{SC}}}{\partial R_{b1}}$ for all four cases:

$$\left(\frac{\partial J_{\mathrm{SC}}}{\partial R_{b1}}\right) \mathrm{specular}, 30\ \mu\mathrm{m} = +0.021\,\mathrm{mA/cm^2}/\%_{\mathrm{abs}}$$

$$\left(\frac{\partial J_{SC}}{\partial R_{b1}}\right) \mathrm{Lambertian}, 30\ \mu\mathrm{m} = +0.019\,\mathrm{mA/cm^2}/\%_{\mathrm{abs}}$$

$$\left(\frac{\partial J_{\mathrm{SC}}}{\partial R_{b1}}\right) \mathrm{specular}, 180\ \mu\mathrm{m} = +0.013\,\mathrm{mA/cm^2}/\%_{\mathrm{abs}}$$

$$\left(\frac{\partial J_{\mathrm{SC}}}{\partial R_{b1}}\right) \mathrm{Lambertian}, 180\ \mu\mathrm{m} = +0.011\,\mathrm{mA/cm^2}/\%_{\mathrm{abs}}.$$

A critical difference between these relationships and that of previously published values relating IBR to J_{SC} are that these values are given with respect to R_{b1} rather than a lumped IBR parameter (R_b in the case of [24]) that is an aggregate of $R_{b1}, R_{b2}, \ldots, R_{bn}$. The impact of a lumped IBR value on J_{SC} is expected to be higher than only R_{b1}, since the overall light trapping capability of a cell (Z) is a function of the reflectance for each bounce and not just R_{b1}. The value in decoupling R_{b1} from the other IBR parameters is related to the aforementioned observation that reflectance at the rear interface is much more dependent on dielectric thickness at relatively low angles of incidence (e.g., $<$40°) when compared with higher angles (e.g., $\approx$60°, which is a commonly assumed value for $\theta_2, \ldots, \theta_n$).

V. Conclusion

In conclusion, the IBR has been modeled as a function of dielectric-layer thickness and the backside angle of incidence at the Si–dielectric interface. Single- and double-layer dielectric backside coatings have been considered, using AlO_x, SiN_x, TiO_2, and SiO_2. The reflectance contour plots, which are calculated using the transfer matrix method, clearly show three critical regions with respect to the backside angle of incidence; for these configurations, $\theta_1 < \theta_c$; θ_1 near θ_c; and $\theta_1 > \theta_c$, where θ_c is the critical angle of the Si–dielectric interface. Experimental reflectance data have also been collected for optically smooth and textured (frontside) substrates, to compare the escape reflectance for the various dielectric coating configurations. The results of the measured escape reflectance data support the conclusions that are derived from the modeling. For the double-layer coatings with a thicker second layer, the lossy second region of the reflectance contour plots (θ_1 near θ_c) is shifted to either higher angles of incidence (for SiN_x and TiO_2) or lower angles (for SiO_2). This affect could play an important role in the IBR of encapsulated cells with backside dielectric configurations.

Future work will be oriented toward gathering experimental data on encapsulated test samples and actual PERC cells, as well as looking at the impact of an intermediate, low index dielectric layer between the passivation layer (i.e., AlO_x) and the capping layer (i.e., SiN_x, TiO_2) to increase the internal back reflectance. Future work will also look to further investigate the correlation between IBR and the overall light trapping ability and short-circuit current enhancements of PERC cells by modeling escape reflection and taking into account the effects of surface roughness, frontside texture, free carrier absorption, and the actual complex refractive index of screen-printed Al pastes. The motivation for this study is to better understand the effect of these various parameters on the overall performance of PERC cells.

Acknowledgment

The authors would like to thank Y. P. Botchak from the University of Konstanz for assistance with the deposition of Al via thermal evaporation, J. Sun of J. A. Woollam for assistance with the spectroscopic ellipsometry measurements of the PECVD SiN_x films on textured substrates, and G. Mahnke from Gebr. Schmid for assistance with the spectroscopic ellipsometry measurements of the APCVD oxide films. They would also like to thank K. R. McIntosh for helpful discussions regarding the OPAL 2 calculator and the general insight provided on solar cell optics and M. G. Moharam for helpful insight regarding the TMM calculations.

References

[1] M. A. Green, "Limits on the open-circuit voltage and efficiency of silicon solar cells imposed by intrinsic Auger processes," *IEEE Trans. Electron Devices*, vol. 31, no. 5, pp. 671–678, May 1984.

[2] T. Tiedje, E. Yablonovitch, G. D. Cody, and B. G. Brooks, "Limiting efficiency of silicon solar cells," *IEEE Trans. Electron Devices*, vol. 31, no. 5, pp. 711–716, May 1984.

[3] M. J. McCann, K. R. Catchpole, K. J. Weber, and A. W. Blakers, "A review of thin-film crystalline silicon for solar cell applications. Part 1: native substrates," *Solar Energy Mater. Solar Cells*, vol. 68, pp. 135–171, 2001.

[4] K. R. Catchpole, M. J. McCann, K. J. Weber, and A. W. Blakers, "A review of thin-film crystalline silicon for solar cell applications—Part 2:

This article has been accepted for inclusion in a future issue of this journal. Content is final as presented, with the exception of pagination.

Foreign substrates," *Solar Energy Mater. Solar Cells*, vol. 68, pp. 173–215, 2001.

[5] G. P. Willeke, "Thin crystalline silicon solar cells," *Solar Energy Mater. Solar Cells*, vol. 72, pp. 191–200, 2002.

[6] X. F. Brun and S. N. Melkote, "Analysis of stresses and breakage of crystalline silicon wafers during handling and transport," *Solar Energy Mater. Solar Cells*, vol. 93, pp. 1238–1247, 2009.

[7] A. Schneider, C. Gernards, P. Fath, E. Bucher, R. J. S. Young, J. A. Raby, and A. F. Carroll, "Bow reducing factors for thin screenprinted mc-Si solar cells with Al BSF," in *Proc. 29th IEEE Photovoltaic Spec. Conf.*, New Orleans, LA, 2002, pp. 336–339.

[8] B. Hoex, J. J. H. Gielis, M. C. M. van de Sanden, and W. M. M. Kessels, "On the c-Si surface passivation mechanism by the negative-charge-dielectric Al_2O_3," *J. Appl. Phys.*, vol. 104, pp. 113703-1–113703-7, 2008.

[9] H. M. Branz, C. W. Teplin, M. J. Romero, I. T. Martin, Q. Wang, K. Alberi, D. L. Young, and P. Stradins, "Hot-wire chemical vapor deposition of epitaxial film crystal silicon for photovoltaics," *Thin Solid Films*, vol. 519, pp. 4545–4550, 2011.

[10] T. Dullweber, S. Gatz, H. Hannebauer, T. Falcon, R. Hesse, J. Schmidt, and R. Brendel, "Towards 20% efficient large-area screen-printed rear-passivated silicon solar cells," *Progress Photovoltaics: Res. Appl.*, vol. 20, no. 6, p. 630—638, 2011.

[11] B. Vermang, H. Goverde, L. Tous, A. Lorenz, P. Choulat, J. Horzel, J. John, J. Poortmans, and R. Mertens, "Approach for Al_2O_3 rear surface passivation of industrial p-type Si PERC above 19%," *Progress Photovoltaics: Res. Appl.*, vol. 20, pp. 269–273, 2012.

[12] M. A. Green, "Self-consistent optical parameters of intrinsic silicon at 300 K including temperature coefficients," *Solar Energy Mater. Solar Cells*, vol. 92, pp. 1305–1310, 2008.

[13] G. Dingemans and W. M. M. Kessels, "Status and prospects of Al_2O_3-based surface passivation schemes for silicon solar cells," *J. Vacuum Sci. Technol. A: Vacuum, Surfaces, Films*, vol. 30, pp. 040802-1–040802-27, 2012.

[14] L. E. Black and K. R. McIntosh, "Surface passivation of c-Si by atmospheric pressure chemical vapor deposition of Al_2O_3," *Appl. Phys. Lett.*, vol. 100, pp. 202107-1–202107-5, 2012.

[15] B. Hoex, S. B. S. Heil, E. Langereis, M. C. M. van de Sanden, and W. M. M. Kessels, "Ultralow surface recombination of c-Si substrates passivated by plasma-assisted atomic layer deposited Al_2O_3," *Appl. Phys. Lett.*, vol. 89, pp. 042112-1–042112-3, 2006.

[16] T. Lauerman, T. Lüder, S. Scholz, B. Raabe, G. Hahn, and B. Terheiden, "Enabling dielectric rear side passivation for industrial mass production by developing lean printing-based solar cell processes," in *Proc. 35th IEEE Photovoltaic Spec. Conf.*, Honolulu, HI, 2010, pp. 28–33.

[17] P. Saint-Cast, J. Benick, D. Kania, L. Weiss, M. Hofmann, J. Rentsch, R. Preu, and S. W. Glunz, "High-efficiency c-Si solar cells passivated with ALD and PECVD aluminum oxide," *IEEE Electron Devices Lett.*, vol. 31, no. 7, pp. 695–697, Jul. 2010.

[18] J. Schmidt, A. Merkle, R. Brendel, B. Hoex, M. C. M. V. de Sanden, and W. M. M. Kessels, "Surface passivation of high-efficiency silicon solar cells by atomic-layer-deposited Al_2O_3," *Progress Photovoltaics: Res. Appl.*, vol. 16, pp. 461–466, 2008.

[19] A. Lorenz, J. John, B. Vermang, E. Cornagliotti, and J. Poortmans, "Comparison of illumination level dependency and rear side reflectance of PERC type cells with different dielectric passivation stacks," in *Proc. 26th Eur. Photovoltaic Solar Energy Conf.*, Hamburg, Germany, 2011.

[20] J. H. Petermann, D. Zielke, J. Schmidt, F. Haase, E. G. Rojas, and R. Brendel, "19%-efficient and 43 μm-thick crystalline Si solar cell from layer transfer using porous silicon," *Progress Photovoltaics: Res. Appl.*, vol. 20, pp. 1–5, 2012.

[21] S. Gatz, H. Hannebauer, R. Hesse, F. Werner, A. Schmidt, T. Dullweber, J. Schmidt, K. Bothe, and R. Brendel, "19.4%-efficient large-area fully screen-printed silicon solar cells," *Physica status solidi (RRL) - Rapid Res. Lett.*, vol. 5, pp. 147–149, 2011.

[22] K. O. Davis, H. P. Seigneur, K. Jiang, C. Demberger, H. Zunft, H. Haverkamp, D. Habermann, and W. V. Schoenfeld, "Optical modeling of the internal back reflectance of various c-Si dielectric stacks featuring AlO_x, SiN_x, TiO_2, and SiO_2," in *Proc. 38th IEEE Photovoltaic Spec. Conf.*, Austin, TX, 2012, pp. 1032–1035.

[23] P. A. Basore, "Extended spectral anlaysis of internal quantum efficiency," in *Proc. 23rd IEEE Photovoltaic Spec. Conf.*, Louisville, KY, 1993, pp. 147–152.

[24] D. Kray, M. Hermle, and S. W. Glunz, "Theory and experiments on the back side reflectance of silicon wafer solar cells," *Progress Photovoltaics: Res. Appl.*, vol. 16, pp. 1–15, 2008.

[25] M. A. Green, "Silicon Solar Cells: Adv. Principles Practice," in *Austrailia: Centre for Photovoltaic Devices and Systems*. Sydney, Austalia: University of New South Wales, 1995, pp. 96–97.

[26] A. Yariv and P. Yeh, *Photonics: Optical Electronics in Modern Communications*, 6th ed. London, U.K.: Oxford Univ. Press, 2007.

[27] E. D. Palik, *Handbook of Optical Constants of Solids*. Orlando, FL: Academic, 1985, p. 759.

[28] P. Kumar, M. K. Wiedmann, C. H. Winter, and I. Avrutsky, "Optical properties of Al_2O_3 thin films grown by atomic layer deposition," *Appl. Opt.*, vol. 48, pp. 5407–5412, 2009.

[29] B. S. Richards, "Single-material TiO2 double-layer antireflection coatings," *Solar Energy Mater. Solar Cells*, vol. 79, pp. 369–390, 2003.

[30] E. D. Palik, *Handbook of Optical Constants of Solids*. Orlando, FL: Academic, 1985, pp. 397–400.

[31] S. C. Baker-Finch and K. R. McIntosh, "Reflection distributions of textured monocrystalline silicon: Implications for silicon solar cells,". (to be published). *Progress Photovoltaics: Res. Appl.*, to be published.

[32] S. C. Baker-Finch and K. R. McIntosh, "Reflection of normally incident light from silicon solar cells with pyramidal texture," *Progress Photovoltaics: Res. Appl.*, vol. 19, pp. 406–416, 2011.

[33] K. R. McIntosh and S. C. Baker-Finch, "OPAL 2: Rapid optical simulation of silicon solar cells," in *Proc. 38th IEEE Photovoltaic Spec. Conf.*, Austin, TX, 2012, pp. 265–271.

[34] P. Yeh, *Optical Waves in Layered Media*. Hoboken, NJ: Wiley, 2005.

[35] F. Werner, B. Veith, D. Zielke, L. Kühnemund, C. Tegenkamp, M. Seibt, R. Brendel, and J. Schmidt, "Electronic and chemical properties of the c-Si/Al_2O_3 interface," *J. Appl. Phys.*, vol. 109, pp. 113701-1–113701-6, 2011.

[36] V. A. Popovich, M. Janssen, I. M. Richardson, T. van Amstel, and I. J. Bennett, "Microstructure and mechanical properties of aluminum back contact layers," in *Proc. 24th Eur. Photovoltaic Solar Energy Conf. Exhib.*, Hamburg, Germany, 2009, pp. 1453–1458.

[37] J. Isenberg and W. Warta, "Free carrier absorption in heavily doped silicon layers," *Appl. Phys. Lett.*, vol. 84, pp. 2265–2267, 2004.

[38] P. Campbell and M. A. Green, "Light trapping properties of pyramidally textured surfaces," *J. Appl. Phys.*, vol. 62, pp. 243–249, 1987.

[39] K. R. McIntosh, R. Shaw, and J. E. Cotter, "Light trapping in SunPower's A-300 solar cells," in *Proc. 19th Eur. Photovoltaic Solar Energy Conf.*, Paris, France, 2004, pp. 844–847.

Author's photographs and biographies not available at the time of publication.